SAXS reveals the molecular basis underlying pH-driven G3BP1 conformational dynamics: implications for stress granule formation

Xiao Han,[1,9] Renhua Sun,[1,9] Melissa A. Graewert,[2] Qianyu Zhou,[3] Tom Resink,[1] Clement E. Blanchet,[2] Hans-Gustaf Ljunggren,[4] Evren Alici,[5,6] Gerald McInerney,[7] Marianne Farnebo,[3] Dmitri Svergun,[2,8,]** and Adnane Achour[1,10,]*

[1] Science for Life Laboratory, Department of Medicine Solna, Karolinska Institute Solna, 17165, Sweden, & Division of Infectious Diseases, Karolinska University Hospital, Stockholm, 17177, Sweden.
[2] European Molecular Biology Laboratory EMBL, Hamburg Unit, c/o DESY, 22607, Hamburg, Germany.
[3] Department of Oncology and Pathology, Karolinska Institute, Stockholm, 17177, Sweden.
[4] Center for Infectious Medicine, Department of Medicine Huddinge, Karolinska Institute, Huddinge 14152, Sweden.
[5] Centre for Hematology and Regenerative Medicine, Department of Medicine Huddinge, Karolinska Institute, Huddinge 14183, Sweden.
[6] Hematology Center, Karolinska University Hospital, Huddinge 14183, Sweden.
[7] Department of Microbiology, Tumor and Cell Biology, Karolinska Institutet, Stockholm, 17165, Sweden.
[8] BIOSAXS GmbH, c/o DESY, 22607, Hamburg, Germany.
[9] These authors contributed equally.
[10] Lead contact
** Correspondence: svergun@biosaxs.com (D.S.)
* Correspondence: adnane.achour@ki.se (A.A.)

Summary

Stress granules (SGs) are cytoplasmic condensates of proteins and RNAs that form in response to cellular stress, playing a critical role in protecting cells during adverse conditions. G3BP proteins act as a central node and molecular switch in SG assembly. Growing evidence indicates that conformational changes in G3BP1 mediate its phase separation competence. However, the mechanistic basis underlying how G3BP conformational dynamics contribute to SG formation has remained elusive. Here, we demonstrate that the G3BP1 homodimer adopts both distinct expanded and compact conformations in solution, with transitions finely modulated by physiological changes in ionic strength and pH. Notably, the G3BP1(ΔRGG) deletion mutant, which is SG-incompetent, abolishes environmentally induced conformational transitions, underscoring the pivotal regulatory role of the RGG domain in G3BP1 dynamics. Additionally, G3BP1 can undergo RNA-independent phase separation at pH 6. Our findings establish a structural framework that connects the conformational plasticity of G3BP1 to its capacity for condensate assembly. We propose that the interplay between intrinsically disordered regions (IDRs), regulated by pH-driven conformational dynamics of G3BP1, finely tunes the threshold for initial granule assembly. These insights significantly enhance our understanding of SG dynamics and provide a mechanistic foundation for investigating how environmental stress conditions influence SG formation and function.

Keywords

Stress granules, G3BP1, conformational dynamics, condensate, phase separation, intermolecular RNA interaction, intrinsically disordered region

Introduction

Eukaryotic cells harbor a wide range of dynamic membrane-less organelles known as ribonucleoprotein (RNP) granules.[1-4] Among these, stress granules (SGs) are cytoplasmic RNP assemblies that primarily form in response to various physiological and pathological conditions, including hypoxia, viral infection, oxidative stress, osmotic stress, and heat-shock.[5-7] SGs play a crucial role in the shutdown of translation during stress and in the regulation of mRNA stability, to maintain cellular homeostasis and promote cell survival. Dysregulation of SGs has been implicated in cancer, viral infections, and neurodegenerative diseases.[8-13] Growing evidence indicates that SGs significantly contribute to chemoresistance and resistance to immunotherapy in various cancer cells.[14-17] Therefore, a thorough understanding of the molecular mechanisms underlying SG assembly holds promise for the development of novel therapeutic strategies in antiviral treatment and cancer management.[18-20]

Previous studies have indicated that SG formation is initiated by the sudden release of mRNAs from polysomes upon translational arrest.[21-24] The GTPase-activating protein SH3 domain-binding proteins (G3BP1, G3BP-2a and G3BP-2b, here collectively referred to as G3BP) play a crucial role in the core network of proteins that regulate SG formation.[25-28] G3BP recognizes long, unfolded single-stranded RNA molecules, consequently triggering condensate formation.[25,29] Specifically, G3BP-RNA condensates are highly sensitive to changes in salt concentrations, dissolving as salt levels increase.[25,26] G3BP features a nuclear transport factor 2-like (NTF2L) domain at its N-terminus, followed by a highly negatively charged acidic domain (also called IDR1, residues 143-225), a positively charged proline-rich domain (PxxP or IDR2, residues 226-334), an RNA-binding domain (RBD) containing an RNA recognition motif (RRM), and an arginine-glycine repeat (RGG) region (residues 411-466), that comprises IDR3.[27,30,31] The NTF2L and RGG domains are indispensable for SG assembly, as deletion mutants G3BP1(ΔNTF2L) and G3BP1(ΔRGG) fail to form condensates in the presence of RNA.[27,29,32] Although considerable attention has been given to structural studies of the NTF2L domain in complex with short linear motifs (SLiMs)[33-35] derived from viral non-structural protein 3 (nsP3),[36] cytoplasmic activation/proliferation-associated protein 1 (Caprin-1)[37] and the nucleoprotein associated with the severe acute respiratory syndrome coronavirus 2,[38] the IDR domains of G3BP1 are increasingly recognized as key contributors to condensate formation through liquid-liquid phase separation (LLPS).[26,29,39] *In vitro* LLPS assays, cell-based SG studies, and deletion mutant analyses indicate that interactions among the three IDRs in G3BP1 can directly regulate its intrinsic propensity for LLPS.[25,26]

G3BP1 granules assemble rapidly in response to acute stress and disassemble within minutes to hours, once normal conditions are restored after stress removal.[40,41] Growing evidence indicates that aging and neurodegenerative diseases are associated with SG dysfunction, with impaired disassembly of these granules implicated in the onset of neurodegeneration.[13,42-44] Despite these associations, the regulatory mechanisms that govern SG dynamics remain poorly understood. A recent study has shown that rapidly assembled G3BP1 condensates, driven by a sudden localized pH drop, can act as stabilizers, plugging and stabilizing damaged endolysosomal membranes. This process facilitates endomembrane repair, helping to maintain cellular integrity under stress conditions.[45] It should be noted that a significantly lower threshold for *in vitro* phase separation is required at a pH below

6.5, compared to the minimal fraction of G3BP1 condensates at neutral pH.[25] Additionally, previous *in silico* and biophysical studies suggested that the molecular dimensions of G3BP1 expanded into a more extended conformation as salt concentrations increased.[25,26] G3BP1-RNA condensates dissolve upon increase of NaCl concentrations from 30 mM to 280 mM,[25] suggesting a connection between an extended conformation of G3BP1 and the dissolution of G3BP1-RNA condensates. These experimental observations contradict the previous model, which proposed that G3BP1 maintains a compact autoinhibitory conformation and switches to an expanded pro-SG conformation in response to stress-induced excess mRNA release.[25,26] How G3BP1 conformation is affected by environmental conditions, and the connection between its conformational dynamics and SG assembly/disassembly remains to be elucidated. A significant gap lies in the absence of a comprehensive structural description of G3BP, primarily due to the predicted high flexibility of its IDRs.

Building on existing functional analyses of G3BP and structural studies of NTF2L/SLiMs,[33,34,36,38] we employed size-exclusion chromatography-coupled SAXS (SEC-SAXS) to determine the overall shapes of full length G3BP1 at different solvent conditions, and *in vitro* LLPS assays to investigate the molecular relationship between G3BP1 conformation and SG dynamics. Our results allowed us to visualize the topological features of the dimeric full-length G3BP1 in solution, revealing that dimeric G3BP1 adopts a more organized conformation compared to AlphaFold 2 predictions.[46,47] Importantly, G3BP1 shifted to a significantly more compact state at decreased salt concentration and pH values, as indicated by a pronounced reduction in radius of gyration (R_g) and by the reconstructed shapes. Additionally, the deletion of the RGG domain abolished this conformational transition, demonstrating the key regulatory role of RGG on the functional capacity of G3BP1. Our biophysical studies demonstrated that the condensation of G3BP1 was greatly affected by environmental factors and directly correlated with its conformational dynamics. We propose that the conformational dynamics of G3BP1, finely tuned by environmental conditions, can mediate SG assembly or disassembly.

Results

G3BP1 forms an elongated homodimer with well-defined and ordered domains

The relationship between the intrinsic molecular properties of G3BP1 and its key regulatory roles in SG formation remains poorly understood. It has been hypothesized that the extensive presence of IDRs in G3BP1 may hinder the clear determination of its three-dimensional structure. Indeed, the sequence and domain organization of G3BP1 reveal at least three highly disordered IDRs (**Figure S1A**), spanning large segments of the acidic, PxxP, and RGG regions (**Figure 1A**). While AlphaFold 2 predicts the structures of the NTF2L dimer and RRM domains with high confidence, it shows significant uncertainty regarding their spatial relationship. Other regions are primarily represented as random loops (**Figure S1B**). Despite the large fraction of predicted disordered regions, we successfully purified recombinant full-length G3BP1. Dynamic light scattering (DLS) analysis revealed a dimer peak with a hydrodynamic radius (Rh) of 8.2 nm (± 0.1 nm), and a polydispersity index (PI) value of 0.2, indicating a high degree of monodispersity (**Figure S1C**).

We employed SEC-SAXS to further analyze full-length G3BP1 in solution at pH 7.5 (**Figure 1**). The estimated molecular weight of 119 kDa (**Table 1**), derived from the scattering frames averaged across the SEC profile, was approximately twice that of the G3BP1 monomer (theoretical Mw 52.5 kDa). *In vitro*, purified G3BP1 primarily forms dimers, with no evidence of higher-order oligomeric species in solution (**Figure S1C**). This observation is consistent with previous multi-angle light scattering and analytical ultracentrifugation studies.[26] The SAXS measurements yielded an R_g of 7.2 nm and a maximum dimension (D_{max}) of 32 nm **(Table 1)**, both indicative of an extended conformation for full-length G3BP1. The pair distance distribution function, p(r), reveals a skewed shape, further confirming that G3BP1 adopts a highly elongated molecular structure (**Figure 1C**).

To independently determine the low-resolution three-dimensional structure of full-length G3BP1, we constructed *ab initio* and hybrid rigid-body models from the SEC-SAXS data. P2 symmetry was applied throughout all calculations, reflecting the dimeric nature of G3BP1 in solution. The *ab initio* model of G3BP1, reconstructed using DAMMIF,[48] revealed an elongated particle with a bulky central node and two lateral extensions (**Figure 1D,** upper inset). The theoretical scattering of this overall shape closely matched the experimental data, yielding a χ^2 value of 0.99 (black line in **Figure 1D**).

To further explore the molecular architecture of G3BP1, hybrid rigid-body models were generated from the scattering data using CORAL.[49] The structure of a G3BP monomer incorporated the crystal structure of the NTF2L homodimer (residues 10-144, PDB ID: 6TA7)[37] and a molecular model of the globular RRM domain (residues 343-417), predicted using AlphaFold 2. The remaining G3BP1 segments were represented as chains of dummy residues. Multiple independent runs reproducibly converged on similar overall shapes, with only minor variations observed in the interdomain contacts and loop arrangements. The curves computed from the hybrid models agreed well with the experimental data, yielding a low discrepancy χ^2 value of about 1.28 (red line in **Figure 1D).** An overlay of a typical hybrid model with the *ab initio* reconstruction further emphasizes the overall good agreement between the two independent analysis approaches (**Figure 1D,** lower inset).

The SAXS-derived hybrid models enabled the identification of specific topological features in full-length G3BP1. The central section of the G3BP1 envelope corresponds to the NTF2L dimer and the adjacent acidic domains, flanked by the PxxP, RRM, and RGG domains, which extend in opposite directions (**Figure 1D**). Repeated CORAL reconstructions and the overall shape derived from the experimental data suggest that the three large IDRs adopt compact conformations in solution at pH 7.5. Notably, the G3BP1 homodimer is slightly bent at the distal ends of each wing, formed by the RGG, RRM, and PxxP domains. The SAXS data and the structural models have been deposited into the Small Angle Scattering Biological Data Bank (SASBDB[50]) (**Table 1 and STAR Methods**).

The NTF2L homodimer domain takes a central position within the head-to-head antiparallel G3BP1 dimer

To validate the central position of the NTF2L homodimer within full-length G3BP1, we generated and isolated the NTF2L domain alone, for which crystal structures have been previously determined by both our research group and others.[36-38]

Additionally, we constructed a truncated version comprising NTF2L and the IDR1-containing acidic domain, henceforth referred to as NTF2LA (**Figure 2A**). SEC-SAXS data collected for both NTF2L and NTF2LA revealed that NTF2L adopts a globular shape, whereas NTF2LA exhibits an elongated, partially unfolded conformation (**Figure 2B**). However, NTF2LA remains significantly shorter than full length G3BP1 (**Figure 2C and Table 1**). *Ab initio* models were subsequently calculated for both constructs (**Figure 2D**). The globular shape obtained for NTF2L closely matched the previously determined crystal structure of the NTF2L dimer (**Figure 2D,** light gray). Similarly to full-length G3BP1, the *ab initio* model of NTF2LA displayed a bulkier central domain, comparable in size to the NTF2L dimer. While the ends of NTF2LA appeared partially unfolded, the overall shape was consistent with the presence of an acidic IDR1 domain at each terminus (**Figures 2D,** dark gray **and S2C**).

These findings ruled out the possibility of a parallel dimer formation for G3BP1, as such a dimer would appear with a significantly thicker and shorter shape than the observed NTF2LA envelope. Furthermore, the available space at each end of the envelope would be insufficient to accommodate the NTF2L dimer. Taken together, these results demonstrate that G3BP1 forms an antiparallel dimer in a head-to-head configuration, with the NTF2L homodimer occupying a central position within the overall structure of full-length G3BP1 (**Figure 1D**). Importantly, the potentially highly flexible and unstructured IDRs appear to be well-organized adjacent to the central NTF2L and RRM domains, contributing to the overall compactness of each domain in full-length G3BP1.

Lower ionic strength and pH value increase the compactness of G3BP1

Previous studies have suggested that a decrease in pH and an increase in salt concentration are associated with the conformational expansion of G3BP1.[25,26] To investigate the impact of solution conditions on G3BP1 conformation, two additional SEC-SAXS runs were performed (**Figure 3A**). The full-length protein was first incubated in a buffer with reduced salt concentration (from 150 to 50 mM NaCl) and thereafter in a buffer with an additional decrease in pH (from 7.5 to 6.0).

Comparison of the three normalized Kratky plots exhibited a leftward peak shift, indicating a reduced conformational flexibility (**Figure 3B**). This compaction was further corroborated by a reduction in R_g, from 7.2 to 6.6 nm and the p(r) function also demonstrated a decrease in D_{max} from 32 to 29 nm (**Table 1**) following reduction in NaCl concentration (**Figure 3C**). Furthermore, *ab initio* models indicated that G3BP1 became significantly more compact when the NaCl concentration was lowered (**Figure 3D, i and ii**). These findings suggest that electrostatic interactions contribute to a measurable contraction of full-length G3BP1 when salt concentration is reduced.

Notably, in contrast to a previous report,[25] further reduction in pH to 6.0 resulted in an additional decrease in R_g and D_{max} to 5.2 nm and 23 nm, respectively, indicating an even more compact shape (**Figure 3D, iii and Table 1**). This substantial reduction in size is evident in the *ab initio* models of full-length G3BP1 under different environmental conditions (**Figure 3D**). These observations demonstrate that environmental factors, such as ionic strength and pH, regulate the conformational dynamics of G3BP1.

The compact conformation of G3BP1 lowers the threshold for *in vitro* phase separation

Next, we investigated how environmentally induced conformational changes in G3BP1 influence SG assembly and disassembly. To this end, we purified full-length GFP-linked G3BP1 and used fluorescence microscopy to monitor the formation of G3BP1-RNA condensates under identical buffer conditions as those in the SAXS measurements. This approach allowed us to directly correlate G3BP1 conformational changes with its LLPS capacity.

At pH 7.5 and in the absence of RNA, GFP-G3BP1 was evenly distributed in solution across a range of NaCl concentrations (**Figures 3E and F**). Consistent with previous reports,[25,26] the formation of visible fluorescent droplets after RNA addition was dependent on the salt concentration. Spherical G3BP1-RNA condensates were observed at pH 7.5 and 50 mM NaCl, but not at 150 mM NaCl (**Figure 3E**), demonstrating that lower ionic strength increases G3BP1´s ability to form condensates with RNA. As expected, no condensates were detected at 300 mM NaCl (**Figure S3A**). We then monitored LLPS dynamics by titrating NaCl into pre-formed fluorescent condensates. The G3BP1-RNA condensates rapidly disassembled when the NaCl concentration was increased to 150 mM (**Figure 3F**), indicating a reversible, environmentally regulated phase separation.

A greater number and larger size of G3BP1-RNA condensates were observed at pH 6 and 50 mM NaCl (**Figure 3E,** lower right panel), which corresponds to conditions where G3BP1 adopts a more compact conformation (**Figure 3Diii**). Surprisingly, we also observed homotypic G3BP1 condensates forming through phase separation in the absence of RNA, albeit smaller in size compared to G3BP1-RNA condensates (**Figure 3E,** upper right panel).

To exclude the possibility that the GFP-tag influenced LLPS formation, we repeated the assays using untagged G3BP1. Although a higher concentration of G3BP1 (25 µM) was required to visualize G3BP1-RNA condensates, the results were consistent with previous fluorescence data at pH 7.5; lower NaCl levels enhanced condensate formation, while phase separation was inhibited at 300 mM NaCl (**Figure S3B**). Overall, these findings indicate that the compact conformation of G3BP1 promotes LLPS more efficiently.

Full-length G3BP1 undergoes both RNA-dependent and RNA-independent phase separation at pH 6.0

SAXS analysis of G3BP1 at pH 6.0 and 50 mM NaCl revealed an even more compact overall conformation, with nearly a 20% size reduction in the *ab initio* model compared to pH 7.5 (**Figure 3D and Table 1**). To further explore the relationship between G3BP1 conformational changes and its LLPS capacity, we closely examined the *in vitro* phase separation behavior of G3BP1 at pH 6.0 using fluorescence microscopy. At 50 mM NaCl, G3BP1 and RNA rapidly formed visible droplets within minutes of mixing (**Figure 4A**), which were larger than those observed at pH 7.5 and 50 mM NaCl (**Figure 3E**). Increasing salt concentration to 150 mM further promoted the formation of G3BP1-RNA condensates (**Figure 4A**). Interestingly, even at 300 mM NaCl, condensates remained present, though their size was notably reduced (**Figures 4A and S4A**). These findings suggest that

G3BP1-RNA condensate formation is maximized under acidic conditions at physiological (or lower) salt concentrations, which may reflect cytoplasmic acidification triggered by various stress signals[51-53] and aging-related diseases[54,55]. Notably, the condensates induced by pH reduction were reversible: both the number and size of G3BP1-RNA condensates significantly decreased when the pH was titrated from 6.0 to 7.5 (**Figure S4A**).

Unexpectedly, G3BP1 also formed visible condensates at pH 6.0 in the absence of RNA (**Figures 3E and 4A**). These RNA-independent droplets were significantly reduced at 150 mM NaCl, and no droplets were observed at 300 mM NaCl (**Figure 4A,** upper right panel). Similar results were obtained using untagged full-length G3BP1 (**Figure S4B**). These findings suggest that G3BP1 can spontaneously undergo RNA-independent droplet formation at pH 6.0 under varied salt concentrations (50 to 150 mM). This phenomenon may be relevant to recent findings showing that a sudden localized decrease in pH (from 7.5 to below 6.5) drives rapid formation of G3BP1 condensates, which help stabilize ruptured membranes and facilitate efficient repair of damaged endolysosomes.[45] The pH-driven conformational changes in G3BP1 may thus provide a molecular mechanism by which cells use SGs to protect against stress, including pathogen-induced damage, such as that caused by *Mycobacterium tuberculosis*, which disrupts endomembranes to evade innate immune responses.[45,56-58]

DLS reveals distinct G3BP1 oligomerization states at pH 6.0

To investigate the size and aggregation profile of G3BP1 in solution, particularly to confirm the RNA-independent droplets observed in LLPS experiments, we performed DLS analyses. Consistent with previous studies, G3BP1 formed a monodisperse dimeric population at physiological pH 7.5 in the absence of RNA, with a peak size centered at ~8.2 nm (**Figure S3C**). However, at pH 6.0, G3BP1 oligomerization was highly sensitive to salt concentration. DLS detected spontaneous aggregation of G3BP1 into large condensates at 50 mM NaCl, with a peak size of ~500 nm (**Figures 4B and S4C,** red curves). Notably, at 300 mM NaCl, large aggregates were no longer detected, and G3BP1 maintained a dimer peak (**Figures 4B and S4C,** blue curves). Interestingly, at pH 6.0 and 150 mM NaCl, DLS analysis identified three distinct oligomeric states: a dimer peak, a larger aggregate peak, and an intermediate peak ~50 nm, likely representing initial nucleation precursors (**Figures 4B and S4C,** green curves). These results confirm that RNA-independent G3BP1 droplets form under conditions corresponding to those used in our LLPS studies.

Importantly, the DLS data suggest that the oligomeric state of G3BP1 is in a reversible equilibrium, dynamically responding to environmental changes. The formation of large G3BP1 oligomers correlates with LLPS results showing RNA-independent G3BP1 condensates at pH 6.0 and low salt concentration (**Figures 4B and S4C**). Furthermore, RNA significantly lowers the threshold for G3BP1-driven phase separation: RNA-dependent G3BP1 condensates form even at 300 mM NaCl (**Figure 4A,** lower right panel), whereas no droplets are observed in the absence of RNA under the same conditions (**Figure 4A,** upper right panel), and no higher-order G3BP1 oligomers are detected by DLS (**Figures 4B and S4C,** blue curves**)**.

The RGG domain is essential for G3BP1 conformational dynamics and condensation under varying salt and pH levels

Previous studies have suggested that interactions between IDRs play a crucial role in regulating G3BP1-centered SG assembly.[25,26,59] The removal of the RGG domain (ΔRGG) has been shown to prevent SG formation,[29] although this truncated variant retains RNA binding ability *in vitro.*[25] However, the specific contributions of individual IDRs and their structural roles remain poorly understood.

To investigate the role of the RGG domain in G3BP1 conformational dynamics, we generated a truncated variant lacking the RGG domain, termed G3BP1(ΔRGG) (**Figure 5A**). This variant was purified and subjected to SEC-SAXS analysis under the same conditions as full-length G3BP1 (**Figure 5B**). G3BP1(ΔRGG) exhibited a similar degree of compaction as full-length G3BP1 at pH 7.5 and 150 mM NaCl. Both had a D_{max} of ~32 nm and yielded comparable R_g values of 7.4 and 7.2 nm, respectively (**Figures 5Ci, 5Ciii and Table 1**). Moreover, the a*b initio* models of full-length G3BP1 and G3BP1(ΔRGG) each maintained an elongated shape under these buffer conditions (**Figures 5Ci and 5Ciii**)**.** Conversely, G3BP1(ΔRGG), unlike full-length G3BP1, did not undergo compaction after decreasing the pH to 6.0 and NaCl concentration to 50 mM (**Figures 5Ciii and 5Civ**). These findings demonstrate that the RGG domain is critical for regulating the conformational flexibility of G3BP1 in solution under varying pH and salt concentrations.

Systematic LLPS assays were also conducted using tag-free G3BP1(ΔRGG) under similar conditions. Consistent with previous reports,[26,29] no significant droplet formation was observed at neutral pH 7.5 across a broad range of ionic strengths, regardless of RNA presence (**Figure S5A**). Interestingly, small and sparse G3BP1(ΔRGG)-RNA condensates were detected at pH 6.0 and 50 mM NaCl, with more prominent condensates forming at pH 6.0 and 150 mM NaCl. However, at 300 mM NaCl, protein-RNA condensates were barely visible (**Figure 5D**). Unlike full-length G3BP1 (**Figure S4B**), G3BP1(ΔRGG) did not form RNA-independent condensates at pH 6 and 50 mM NaCl (**Figure 5D**). These results indicate that the RGG domain is essential for both RNA-dependent and RNA-independent G3BP1 condensate formation under specific conditions.

DLS analysis of G3BP1(ΔRGG) at pH 6.0 (**Figures 5E and S5C**) showed results comparable to those obtained for full-length G3BP1 (**Figures 4B and S4C**), except that G3BP1(ΔRGG) failed to form large condensates (Rh ~500 nm). Instead, it primarily populated an intermediate state, with an Rh centered around 50 nm at 50 mM NaCl (**Figure 5E**), suggesting that the RGG domain is required for the formation of higher ordered homotypic G3BP1 condensates.

In summary, removal of the positively charged RGG region abrogates the observed transition between G3BP1 conformational states, causing G3BP1(ΔRGG) to retain an elongated shape regardless of variations in salt concentrations and pH values. This behavior coincides with the inability of G3BP1(ΔRGG) to undergo RNA-independent condensate formation at pH 6.0 and 50 mM NaCl (**Figures 5D and 5E**). These findings highlight the essential role of the RGG domain in regulating both the conformational dynamics and the phase separation capacity of G3BP1.

Environmental factors drive G3BP1 domain rearrangements, regulating G3BP1-RNA condensate formation and SG nucleation

To elucidate the molecular mechanisms underlying G3BP1 domain rearrangements and their importance in LLPS, multiple independent experimental-based hybrid models were generated and compared to identify consistent domain arrangements (**Figure S6**). Representative hybrid models were closely aligned with the corresponding *ab initio* shapes (**Figures 6A-E**).

At pH 7.5 and 150 mM NaCl, the RGG, RRM and PxxP regions of full-length G3BP1 extended outward from the central core, which comprises the NTF2L and acidic domains, contributing to an overall elongated shape (**Figures 6A and S6A**). However, as the pH and salt concentration decreased to 6.0 and 50 mM, the hybrid models revealed a spatial rearrangement of G3BP1 domains. Specifically, the RRM and RGG domains moved closer to NTF2L, resulting in a significantly more compact and shorter conformation (**Figures 6B and S6B**). These observations align well with the SAXS-derived decrease in R_g and D_{max} values (**Figure 3B and Table 1**) and the DAMMIF envelopes (**Figure 3D**). A previous study showed that the overall compaction of *in silico*-derived G3BP1 correlated linearly with the spacing between IDR1 and RGG,[26] which is consistent with our hybrid models (**Figures 6A and 6B**).

The domain distribution in G3BP1(ΔRGG) was similar to that of full-length G3BP1 at pH 7.5 and 150 mM NaCl (**Figures 6C and S6C**). However, in contrast to full-length G3BP1, no significant domain reorganization was observed in G3BP1(ΔRGG) when pH and salt concentrations were reduced (**Figures 6D and S6D**).

Mechanism of stress-induced G3BP1 conformational changes

Together with the observed LLPS and DLS results obtained at different salt and pH conditions, the hybrid models of G3BP1 and G3BP1(ΔRGG) provide insights into how environmental factors regulate G3BP1 domain rearrangements, thereby modulating its ability to form condensates with RNA (**Figure 6F**). Under neutral physiological conditions, the G3BP1 dimer adopts an elongated conformation, with the RGG domain extending distally, away from IDR1 (**Figures 6A and 6F**). The highly negatively charged IDR1, which may contain phosphorylated groups, is positioned near NTF2L (**Figure 6A**). This arrangement generates strong electronegative repulsion preventing intermolecular protein/RNA and possibly protein/protein interactions. Consequently, this structural configuration limits G3BP1's ability to form crosslinked condensate networks, placing G3BP1 in a SG-incompetent state.

Upon stress, intracellular pH decreases, promoting G3BP1 compaction. This rearrangement brings the RGG domain closer to the structural center of G3BP1 (**Figure 6B**). The positively charged RGG domain neutralizes the negative charges of IDR1, reducing its repulsive effect on intermolecular RNA-RNA and protein-RNA interactions. As a result, G3BP1 forms a crosslinked protein-RNA network, and these initial condensates may synergistically cooperate with other SG-related proteins containing RNA binding domains, ultimately leading to SG assembly. Notably, G3BP1(ΔRGG) does not undergo such conformational changes under the same conditions (**Figures 6C and 6D**), highlighting the critical role of the RGG domain in dynamic domain rearrangement within G3BP1.

Taken together, the proposed mechanism is strongly supported by experimental SAXS, LLPS and DLS data presented in this study. Our findings reinforce the idea that stress-induced G3BP1 conformational rearrangements enable efficient intermolecular protein-RNA and RNA-RNA interactions, with IDR interplay playing a crucial role in regulating SG dynamics.

Discussion

The dynamic nature of RNP granules is crucial for maintaining the functional flexibility of biological processes, particularly under stress conditions.[6,7,60-62] Dysregulation of these granules, including alterations in their structure and turnover rates, has been linked to severe human diseases, tumor progression, and cancer.[3,4,6,19,51] Previous studies have demonstrated that various stressors can induce intracellular pH fluctuations in mammalian, plant, and microbial cells.[44,51-53,63-66] Moreover, intracellular acidification is intimately linked to aging processes and aging-related neurodegenerative diseases.[44,54,55] In response to stress-induced pH changes, proteins and RNAs undergo LLPS to help cells adapt to adverse environments.[67-69] However, the molecular mechanisms by which pH mediates phase separation remain poorly understood. Since G3BP serves as the central node and molecular switch that triggers SG formation,[26-28,30,62] understanding its structural dynamics is essential for elucidating how cells efficiently assemble SGs in response to various stressors and disassemble them once the stress subsides.

Our SEC-SAXS and biophysical study provides the first structural insight into full-length G3BP1, revealing that it adopts an elongated conformation in solution and assembles into a stable, well-organized dimer. Environmental changes, such as stress-induced intracellular acidification, lead to structural rearrangements of the IDRs, resulting in a significantly more compact G3BP1 conformation. Notably, deletion of the RGG domain disrupts the ability of G3BP1 to undergo conformational rearrangements in response to pH and salt fluctuations, highlighting the RGG region as a critical mediator of G3BP1 conformational flexibility under varying environmental conditions. To our knowledge, these findings provide the first experimentally derived structural model of full-length G3BP1, offering fundamental insights into environment-driven molecular architecture dynamics.

IDRs are essential for maintaining the dynamic nature of SGs

The combination of amino acid composition and the relative positioning of positively and negatively charged residues within IDRs play a key role in regulating LLPS. [70-73] Our findings indicate that the IDR1 and RGG domains play distinct but complementary roles in G3BP1-dependent phase separation dynamics. Deletion of the RGG domain abolishes the conformational dynamics of G3BP1, rendering it unable to undergo LLPS. Previous studies have shown that removal of IDR1 promotes SG assembly at significantly lower G3BP1 concentrations, even at neutral pH, where G3BP1 is not inducing phase separation[25,26] This can be explained by the loss of electrostatic repulsion from negatively charged IDR1, which allows for the formation of higher-order crosslinked G3BP1-RNA network. Additionally, SGs assembled with G3BP1 mutants lacking IDR1 or additional RGG-mimic motifs exhibit significantly reduced dynamics despite their higher efficiency in reconstituting SGs in *G3BP1/2* double knock-out cells.[26,28] Furthermore, a deletion variant lacking the proline-rich IDR2 fails to rescue SG formation in G3BP1/G3BP2 double-knockout cells.[28] Based on our hybrid models, IDR2 spatially separates the IDR1 and RGG regions, with its intrinsic flexibility facilitating the transitions between the compact and expanded G3BP1 conformations. Altogether, these results indicate that the three IDRs in G3BP1 are crucial for SG assembly and disassembly, with each region

evolutionarily preserving distinct, non-redundant roles critical for this biological process.

As previously reported, the intrinsic properties of both G3BP1 and RNA are critical for SG formation,[25,71,74] with positive regulators (e.g., Caprin-1,[37] TIA1[5] and UBAP2L[75]) and the negative regulator (USP10[29]) modulating G3BP1-RNA condensation in response to various biological stresses. Mutations in the RRM (F380D/F382D), which impair RNA binding, abolish SG assembly.[26] Notably, only RNA-dependent LLPS of G3BP1 is influenced by the net charge of the RGG domain, whereas crowding agent-induced LLPS remains unaffected.[26] This underscores the essential interplay between IDRs and RNA in promoting SG assembly *in vivo.*[25,27,28]

Intermolecular RNA-RNA interactions are crucial for promoting higher-order network assembly and lowering the threshold of phase separation.[25,76,77] Our data demonstrate that decreases in pH or salt concentration induce observable changes in the overall conformation of G3BP1. Among these, the RGG region plays a critical role by electrostatically interacting with the negatively charged IDR1, thereby enhancing intermolecular protein-RNA and RNA-RNA interactions necessary for condensate assembly. Recent findings provide further evidence of the critical role of G3BP1-promoted intermolecular RNA-RNA interactions in SG formation.[78,79]

Several studies have shown that phosphorylation of G3BP1 at S149 and S232 within the acidic IDR1 domain reduces its propensity for LLPS.[25,26,28] This suggests that site-specific phosphorylation of IDR1 functions as a natural negative regulator of SG initiation by increasing electrostatic repulsion between RNA molecules and inhibiting intermolecular RNA-protein interactions. Phosphorylated G3BP1 thus remains in an autoinhibited state under normal conditions, helping to stabilize the cellular microenvironment.

Homotypic G3BP1 condensates form through pH-dependent phase separation

A surprising finding in our study is the formation of pH-driven homotypic G3BP1 condensates in the absence of RNA. Both i*n vitro* LLPS and DLS analyses clearly demonstrated the self-assembly of G3BP1 at pH 6.0. Whether this homotypic phase separation of G3BP1 represents a biologically relevant phenomenon remains unclear. However, we cannot exclude that pH-induced homotypic G3BP1 phase separation serves as an initial nucleation core, together with RNA and other SG components, synergistically driving condensate maturation.

Recent studies have demonstrated that in response to lysosomal leakage caused by *Mycobacterium tuberculosis* (Mtb) infection,[57,58] a localized cytosolic pH drop induced G3BP1 condensates, which efficiently plugged and stabilized the damaged endomembrane.[45] Similarly, in the yeast translation termination factor Sup35, an acidic disordered region functions as a stress sensor, triggering the formation of biomolecular condensates under low pH conditions caused by starvation.[69,80] The cellular microenvironment likely dynamically regulates the conformational state of G3BP1, enabling it to adapt its functional roles based on physiological demands.

Conclusion and future perspectives

By integrating complementary structural and biophysical methods, our study reveals the solution conformation of G3BP1 and demonstrates that environmental factors,

such as salt concentration and pH, regulate its conformational dynamics. When intracellular conditions become acidic due to stressors such as nutrient starvation, hypoxia, pathogen infection, or tumorigenesis,[44,51,52,69] G3BP1 adopts a compact conformation. In this state, the RGG domain counteracts the electrostatic repulsion of IDR1, promoting intermolecular RNA-RNA and/or G3BP-RNA interactions, thereby driving early stages of condensation. Our model provides new insights into the molecular mechanisms underlying pH-driven LLPS in cellular adaptation. It offers a structural framework for understanding interactions between G3BP1 and other SG components, potentially extending to other RNP condensates. These results pave the way for designing allosteric inhibitors that modulate G3BP1 conformational transitions, opening potential therapeutic avenues for diseases associated with SG dysregulation.

Limitations of the study

Our study advances the understanding of how environmental factors regulate G3BP1 conformational plasticity and its role in LLPS. However, our findings are primarily based on *in vitro* biophysical and structural analyses, which may not capture the full complexity of SG dynamics in live cells. Despite this fact, it remains challenging to monitor the stress-induced microenvironmental changes and to visualize the G3BP1-directed intermolecular RNA-RNA interactions within cellular systems, due to the inherent intracellular complexity and current technological limitations. Additionally, we demonstrate that both ionic strength and pH influence G3BP1 conformational states and phase separation, but the impact of these changes on interactions with other SG core components, such as UBAP2L, Caprin1, and TIA1, is still unclear. While these interactions are crucial for SG maturation and dynamics, the basis for their regulation by environmental stressors remains unknown. Furthermore, it is not evident whether the observed RNA-independent homotypic G3BP1 condensate formation observed at pH 6 contributes to the early stages of SG nucleation or serves other cellular functions. The physiological relevance of these condensates needs to be explored within different stress contexts, including viral infection and oncogenesis, where SG dysregulation is commonly observed. Addressing these limitations will provide deeper insights into the mechanistic basis of G3BP1-mediated SG assembly and its broader implications in cellular stress responses.

Resource availability

Lead contact

Further information and requests for resources and reagents should be directed to and will be fulfilled by the lead contact, Adnane Achour (adnane.achour@ki.se).

Materials availability

No new reagents were generated in this study.

Data and code availability

All relevant data associated with the published study are present in the paper or the Supplementary Information. The SAXS data generated in this study have been deposited in the SASBDB database (www.sasbdb.org) under accession codes SASDWD8, SASDWE8, SASDWF8, SASDWG8, SASDWH8, SASDWJ8, SASDWK8, SASDWL8.

Acknowledgements

We thank Jodie Lavender, the local coordinator at the beamline Diamond B21, for organizing the SAXS samples delivery. We thank the B21 beamline staff for collecting the SEC-SAXS data. This work was supported by grants from the Swedish Research Council (AA; 2021-05061), The Swedish Cancer Society (AA; 24 3775 Pj O1 H), The King Gustaf V Jubileum Fund (AA; 244092) and the Swedish Cancer and Allergy Foundation (AA; 11338).

Author contributions

A.A., X.H., R.H.S. and D.S. conceptualized the project. X.H. and R.S. cloned, expressed, and purified all protein constructs. X.H. and R.H.S. prepared the SEC-SAXS samples, analyzed the scattering data and prepared the figures. M.A.G., C.E.B. and D.S. supervised and provided help with the analysis of the SEC-SAXS results. X.H. and R.H.S. conducted the LLPS assays in close collaboration with Q.Z. and M.F.; X.H., R.H.S., H.G.L., T.R. and A.A. wrote the manuscript. All authors discussed and commented on the final version. A.A., E.A., D.S., and H.G.L. have acquired all financial support.

Declaration of interests

The authors declare no competing interests.

Table 1 SAXS sample details, data collection, analysis, and 3D modeling details

Sample details and set-up			
Organism	Human		
Source (Catalog No. or reference)	*E. coli*		
SAXS data collection mode	Size exclusion chromatography		
Sample temperature (°C)	15 °C		
In beam sample cell	1.5 mm quartz capillary		
Concentration range (mg/ml)	8 -10		
Sample injection volume, µl	~60		
SEC column type	Cytiva Superdex 200 Increase 3.2/300 column		
SEC flowrate, ml/min	0.075		
SAXS Data collection parameters			
Instrument	B21 beam line, Diamond Light Source (Didcot, UK)		
Detector	EigerX 4M (Dectris)		
Sample to detector distance (m)	3.7		
Wavelength of λ (nm)	0.09464		
s range (nm^{-1})	0.045 – 3.4		
Exposure time (s)	3		
SAS-derived structural parameters (from ATSAS)			
	G3BP1		
Buffer	pH 7.5 150 mM NaCl	pH 7.5 50 mM NaCl	pH 6.0 50 mM NaCl
Data processing	PRIMUS	PRIMUS	PRIMUS
R_g (nm) (from $p(r)$)	7.2 ± 0.1	6.6 ± 0.1	5.2 ± 0.1
R_g (nm) (Reciprocal space)	7.1	6.5	5.2
D_{max} (nm)	32.4	28.7	22.5
Porod volume estimate, V_p (nm^3)	221	218	163
Molecular weight determination (kDa)			
From consensus Bayesian assessment	119 ± 8	125 ± 9	110 ± 7
From protein sequence (dimer)	105	105	105
Ab initio modeling			
Software	Dammin	Dammin	Dammin
chi^2	0.99	1.04	1.05
Rigid body modeling			
Software	Coral	Coral	Coral
X^2	1.28	1.12	2.04
Data and model deposition			
SASBDB IDs	SASDWD8	SASDWE8	SASDWF8

	NTF2L	**NTF2A**	
Buffer	pH 7.5 150 mM NaCl	pH 7.5 150 mM NaCl	pH 6.0 50 mM NaCl
R_g (nm) (from $p(r)$)	2.0 ± 0.002	4.3 ± 0.01	3.9 ± 0.001
R_g (nm) (Reciprocal space)	2.0	4.3	3.9
D_{max} (nm)	6.5	16.2	15.1
Porod volume estimate, V_p (nm^3)	40	108	96
Molecular weight determination (kDa)			
From SAXS	30 ± 1	62 ± 3	60 ± 3
From protein sequence (dimer)	31.8	53.4	53.4
Ab initio *modeling*			
Software	Dammif	Dammif	Dammif
chi^2	1.07	1.07	1.2
Atomistic modeling methods			
Software	SREFLEX		
X^2	1.07		
Data and model deposition			
SASBDB IDs	SASDWG8	SASDWH8	SASDWJ8

	G3BP1(ΔRGG)	
Buffer	pH 7.5, 150 mM NaCl	pH 6.0, 50 mM NaCl
Data processing	PRIMUS	PRIMUS
R_g (nm) (from $p(r)$)	7.4 ± 0.05	6.8 ± 0.06
R_g (nm) (Reciprocal space)	7.4	6.8
D_{max} (nm)	32	31
Porod volume estimate, V_p (nm^3)	226	227
Molecular weight determination (kDa)		
From SAXS	102 ± 10	125 ± 9
From protein sequence (dimer)	94	94
Ab initio modeling		
Software	Dammin	Dammin
chi^2	1.06	0.98
Rigid body modeling		
Software	Coral	Coral
X^2	4.2	4.6
Data and model deposition		
SASBDB IDs	SASDWK8	SASDWL8

References

1. Alberti, S., Gladfelter, A., and Mittag, T. (2019). Considerations and Challenges in Studying Liquid-Liquid Phase Separation and Biomolecular Condensates. Cell *176*, 419-434. 10.1016/j.cell.2018.12.035.
2. Posey, A.E., and Pappu, R.V. (2018). A First Glimpse of Nucleation of Phase Transitions in Living Cells. Mol Cell *71*, 1-3. 10.1016/j.molcel.2018.06.028.
3. Kedersha, N., Ivanov, P., and Anderson, P. (2013). Stress granules and cell signaling: more than just a passing phase? Trends Biochem Sci *38*, 494-506. 10.1016/j.tibs.2013.07.004.
4. Ripin, N., and Parker, R. (2023). Formation, function, and pathology of RNP granules. Cell *186*, 4737-4756. 10.1016/j.cell.2023.09.006.
5. Kedersha, N.L., Gupta, M., Li, W., Miller, I., and Anderson, P. (1999). RNA-binding proteins TIA-1 and TIAR link the phosphorylation of eIF-2 alpha to the assembly of mammalian stress granules. J Cell Biol *147*, 1431-1442. 10.1083/jcb.147.7.1431.
6. Zhou, H., Luo, J., Mou, K., Peng, L., Li, X., Lei, Y., Wang, J., Lin, S., Luo, Y., and Xiang, L. (2023). Stress: functions and mechanisms in cancer. Cell Biosci *13*, 86. 10.1186/s13578-023-01030-6.
7. Cui, Q., Liu, Z., and Bai, G. (2024). Friend or foe: The role of stress granule in neurodegenerative disease. Neuron *112*, 2464-2485. 10.1016/j.neuron.2024.0 granules 4.025.
8. Protter, D.S.W., and Parker, R. (2016). Principles and Properties of Stress Granules. Trends Cell Biol *26*, 668-679. 10.1016/j.tcb.2016.05.004.
9. Advani, V.M., and Ivanov, P. (2020). Stress granule subtypes: an emerging link to neurodegeneration. Cell Mol Life Sci *77*, 4827-4845. 10.1007/s00018-020-03565-0.
10. Gao, X., Jiang, L., Gong, Y., Chen, X., Ying, M., Zhu, H., He, Q., Yang, B., and Cao, J. (2019). Stress granule: A promising target for cancer treatment. Br J Pharmacol *176*, 4421-4433. 10.1111/bph.14790.
11. McCormick, C., and Khaperskyy, D.A. (2017). Translation inhibition and stress granules in the antiviral immune response. Nat Rev Immunol *17*, 647-660. 10.1038/nri.2017.63.
12. Brownsword, M.J., and Locker, N. (2023). A little less aggregation a little more replication: Viral manipulation of stress granules. Wiley Interdiscip Rev RNA *14*, e1741. 10.1002/wrna.1741.
13. Wolozin, B., and Ivanov, P. (2019). Stress granules and neurodegeneration. Nat Rev Neurosci *20*, 649-666. 10.1038/s41583-019-0222-5.
14. Farny, N.G., Kedersha, N.L., and Silver, P.A. (2009). Metazoan stress granule assembly is mediated by P-eIF2alpha-dependent and -independent mechanisms. RNA *15*, 1814-1821. 10.1261/rna.1684009.
15. Franchini, D.M., Lanvin, O., Tosolini, M., Patras de Campaigno, E., Cammas, A., Pericart, S., Scarlata, C.M., Lebras, M., Rossi, C., Ligat, L., et al. (2019). Microtubule-Driven Stress Granule Dynamics Regulate Inhibitory Immune Checkpoint Expression in T Cells. Cell Rep *26*, 94-107 e107. 10.1016/j.celrep.2018.12.014.
16. Garcia, M.A., Carrasco, E., Aguilera, M., Alvarez, P., Rivas, C., Campos, J.M., Prados, J.C., Calleja, M.A., Esteban, M., Marchal, J.A., and Aranega, A. (2011). The chemotherapeutic drug 5-fluorouracil promotes PKR-mediated apoptosis in a p53-independent manner in colon and breast cancer cells. PLoS One *6*, e23887. 10.1371/journal.pone.0023887.
17. Li, H., Lin, P.H., Gupta, P., Li, X., Zhao, S.L., Zhou, X., Li, Z., Wei, S., Xu, L., Han, R., et al. (2021). MG53 suppresses tumor progression and stress granule formation by

modulating G3BP2 activity in non-small cell lung cancer. Mol Cancer *20*, 118. 10.1186/s12943-021-01418-3.
18. Jia, Y., Jia, R., Dai, Z., Zhou, J., Ruan, J., Chng, W., Cai, Z., and Zhang, X. (2024). Stress granules in cancer: Adaptive dynamics and therapeutic implications. iScience *27*, 110359. 10.1016/j.isci.2024.110359.
19. Gupta, N., Badeaux, M., Liu, Y., Naxerova, K., Sgroi, D., Munn, L.L., Jain, R.K., and Garkavtsev, I. (2017). Stress granule-associated protein G3BP2 regulates breast tumor initiation. Proc Natl Acad Sci U S A *114*, 1033-1038. 10.1073/pnas.1525387114.
20. Liu, S., Tian, S., Lin, T., He, X., Eze Ideozu, J., Wang, R., Wang, Y., Yue, D., and Geng, H. (2022). G3BP1 regulates breast cancer cell proliferation and metastasis by modulating PKCzeta. Front Genet *13*, 1034889. 10.3389/fgene.2022.1034889.
21. Mitchell, S.F., and Parker, R. (2014). Principles and properties of eukaryotic mRNPs. Mol Cell *54*, 547-558. 10.1016/j.molcel.2014.04.033.
22. Ivanov, P., Kedersha, N., and Anderson, P. (2019). Stress Granules and Processing Bodies in Translational Control. Cold Spring Harb Perspect Biol *11*. 10.1101/cshperspect.a032813.
23. Brengues, M., Teixeira, D., and Parker, R. (2005). Movement of eukaryotic mRNAs between polysomes and cytoplasmic processing bodies. Science *310*, 486-489. 10.1126/science.1115791.
24. Kedersha, N., Cho, M.R., Li, W., Yacono, P.W., Chen, S., Gilks, N., Golan, D.E., and Anderson, P. (2000). Dynamic shuttling of TIA-1 accompanies the recruitment of mRNA to mammalian stress granules. J Cell Biol *151*, 1257-1268. 10.1083/jcb.151.6.1257.
25. Guillen-Boixet, J., Kopach, A., Holehouse, A.S., Wittmann, S., Jahnel, M., Schlussler, R., Kim, K., Trussina, I., Wang, J., Mateju, D., et al. (2020). RNA-Induced Conformational Switching and Clustering of G3BP Drive Stress Granule Assembly by Condensation. Cell *181*, 346-361 e317. 10.1016/j.cell.2020.03.049.
26. Yang, P., Mathieu, C., Kolaitis, R.M., Zhang, P., Messing, J., Yurtsever, U., Yang, Z., Wu, J., Li, Y., Pan, Q., et al. (2020). G3BP1 Is a Tunable Switch that Triggers Phase Separation to Assemble Stress Granules. Cell *181*, 325-345 e328. 10.1016/j.cell.2020.03.046.
27. Tourriere, H., Chebli, K., Zekri, L., Courselaud, B., Blanchard, J.M., Bertrand, E., and Tazi, J. (2003). The RasGAP-associated endoribonuclease G3BP assembles stress granules. J Cell Biol *160*, 823-831. 10.1083/jcb.200212128.
28. Sanders, D.W., Kedersha, N., Lee, D.S.W., Strom, A.R., Drake, V., Riback, J.A., Bracha, D., Eeftens, J.M., Iwanicki, A., Wang, A., et al. (2020). Competing Protein-RNA Interaction Networks Control Multiphase Intracellular Organization. Cell *181*, 306-324 e328. 10.1016/j.cell.2020.03.050.
29. Kedersha, N., Panas, M.D., Achorn, C.A., Lyons, S., Tisdale, S., Hickman, T., Thomas, M., Lieberman, J., McInerney, G.M., Ivanov, P., and Anderson, P. (2016). G3BP-Caprin1-USP10 complexes mediate stress granule condensation and associate with 40S subunits. J Cell Biol *212*, 845-860. 10.1083/jcb.201508028.
30. Parker, F., Maurier, F., Delumeau, I., Duchesne, M., Faucher, D., Debussche, L., Dugue, A., Schweighoffer, F., and Tocque, B. (1996). A Ras-GTPase-activating protein SH3-domain-binding protein. Mol Cell Biol *16*, 2561-2569. 10.1128/MCB.16.6.2561.
31. Chong, S., Dugast-Darzacq, C., Liu, Z., Dong, P., Dailey, G.M., Cattoglio, C., Heckert, A., Banala, S., Lavis, L., Darzacq, X., and Tjian, R. (2018). Imaging dynamic and selective low-complexity domain interactions that control gene transcription. Science *361*. 10.1126/science.aar2555.

32. Bley, C.J., Nie, S., Mobbs, G.W., Petrovic, S., Gres, A.T., Liu, X., Mukherjee, S., Harvey, S., Huber, F.M., Lin, D.H., et al. (2022). Architecture of the cytoplasmic face of the nuclear pore. Science *376*, eabm9129. 10.1126/science.abm9129.
33. McInerney, G.M. (2015). FGDF motif regulation of stress granule formation. DNA Cell Biol *34*, 557-560. 10.1089/dna.2015.2957.
34. Kristensen, O. (2015). Crystal structure of the G3BP2 NTF2-like domain in complex with a canonical FGDF motif peptide. Biochem Biophys Res Commun *467*, 53-57. 10.1016/j.bbrc.2015.09.123.
35. Vognsen, T., Moller, I.R., and Kristensen, O. (2013). Crystal structures of the human G3BP1 NTF2-like domain visualize FxFG Nup repeat specificity. PLoS One *8*, e80947. 10.1371/journal.pone.0080947.
36. Schulte, T., Liu, L., Panas, M.D., Thaa, B., Dickson, N., Gotte, B., Achour, A., and McInerney, G.M. (2016). Combined structural, biochemical and cellular evidence demonstrates that both FGDF motifs in alphavirus nsP3 are required for efficient replication. Open Biol *6*. 10.1098/rsob.160078.
37. Schulte, T., Panas, M.D., Han, X., Williams, L., Kedersha, N., Fleck, J.S., Tan, T.J.C., Dopico, X.C., Olsson, A., Morro, A.M., et al. (2023). Caprin-1 binding to the critical stress granule protein G3BP1 is influenced by pH. Open Biol *13*, 220369. 10.1098/rsob.220369.
38. Biswal, M., Lu, J., and Song, J. (2022). SARS-CoV-2 Nucleocapsid Protein Targets a Conserved Surface Groove of the NTF2-like Domain of G3BP1. J Mol Biol *434*, 167516. 10.1016/j.jmb.2022.167516.
39. Holehouse, A.S., and Alberti, S. (2025). Molecular determinants of condensate composition. Mol Cell *85*, 290-308. 10.1016/j.molcel.2024.12.021.
40. Hofmann, S., Kedersha, N., Anderson, P., and Ivanov, P. (2021). Molecular mechanisms of stress granule assembly and disassembly. Biochim Biophys Acta Mol Cell Res *1868*, 118876. 10.1016/j.bbamcr.2020.118876.
41. Mateju, D., Eichenberger, B., Voigt, F., Eglinger, J., Roth, G., and Chao, J.A. (2020). Single-Molecule Imaging Reveals Translation of mRNAs Localized to Stress Granules. Cell *183*, 1801-1812 e1813. 10.1016/j.cell.2020.11.010.
42. Baron, D.M., Kaushansky, L.J., Ward, C.L., Sama, R.R., Chian, R.J., Boggio, K.J., Quaresma, A.J., Nickerson, J.A., and Bosco, D.A. (2013). Amyotrophic lateral sclerosis-linked FUS/TLS alters stress granule assembly and dynamics. Mol Neurodegener *8*, 30. 10.1186/1750-1326-8-30.
43. Sidibe, H., Dubinski, A., and Vande Velde, C. (2021). The multi-functional RNA-binding protein G3BP1 and its potential implication in neurodegenerative disease. J Neurochem *157*, 944-962. 10.1111/jnc.15280.
44. Jin, X., Zhou, M., Chen, S., Li, D., Cao, X., and Liu, B. (2022). Effects of pH alterations on stress- and aging-induced protein phase separation. Cell Mol Life Sci *79*, 380. 10.1007/s00018-022-04393-0.
45. Bussi, C., Mangiarotti, A., Vanhille-Campos, C., Aylan, B., Pellegrino, E., Athanasiadi, N., Fearns, A., Rodgers, A., Franzmann, T.M., Saric, A., et al. (2023). Publisher Correction: Stress granules plug and stabilize damaged endolysosomal membranes. Nature *624*, E3. 10.1038/s41586-023-06882-z.
46. Jumper, J., Evans, R., Pritzel, A., Green, T., Figurnov, M., Ronneberger, O., Tunyasuvunakool, K., Bates, R., Zidek, A., Potapenko, A., et al. (2021). Highly accurate protein structure prediction with AlphaFold. Nature *596*, 583-589. 10.1038/s41586-021-03819-2.
47. Varadi, M., Bertoni, D., Magana, P., Paramval, U., Pidruchna, I., Radhakrishnan, M., Tsenkov, M., Nair, S., Mirdita, M., Yeo, J., et al. (2023). AlphaFold Protein Structure

Database in 2024: providing structure coverage for over 214 million protein sequences. Nucleic Acids Research *52*, D368-D375. 10.1093/nar/gkad1011.
48. Franke, D., and Svergun, D.I. (2009). DAMMIF, a program for rapid ab-initio shape determination in small-angle scattering. J Appl Crystallogr *42*, 342-346. 10.1107/S0021889809000338.
49. Petoukhov, M.V., Franke, D., Shkumatov, A.V., Tria, G., Kikhney, A.G., Gajda, M., Gorba, C., Mertens, H.D., Konarev, P.V., and Svergun, D.I. (2012). New developments in the ATSAS program package for small-angle scattering data analysis. J Appl Crystallogr *45*, 342-350. 10.1107/S0021889812007662.
50. Kikhney, A.G., Borges, C.R., Molodenskiy, D.S., Jeffries, C.M., and Svergun, D.I. (2020). SASBDB: Towards an automatically curated and validated repository for biological scattering data. Protein Sci *29*, 66-75. 10.1002/pro.3731.
51. Peppicelli, S., Calorini, L., Bianchini, F., Papucci, L., Magnelli, L., and Andreucci, E. (2024). Acidity and hypoxia of tumor microenvironment, a positive interplay in extracellular vesicle release by tumor cells. Cell Oncol (Dordr). 10.1007/s13402-024-00969-z.
52. Estrella, V., Chen, T., Lloyd, M., Wojtkowiak, J., Cornnell, H.H., Ibrahim-Hashim, A., Bailey, K., Balagurunathan, Y., Rothberg, J.M., Sloane, B.F., et al. (2013). Acidity generated by the tumor microenvironment drives local invasion. Cancer Res *73*, 1524-1535. 10.1158/0008-5472.CAN-12-2796.
53. Joyner, R.P., Tang, J.H., Helenius, J., Dultz, E., Brune, C., Holt, L.J., Huet, S., Muller, D.J., and Weis, K. (2016). A glucose-starvation response regulates the diffusion of macromolecules. Elife *5*. 10.7554/eLife.09376.
54. Bonnet, U., Bingmann, D., Speckmann, E.J., and Wiemann, M. (2018). Aging is associated with a mild acidification in neocortical human neurons in vitro. J Neural Transm *125*, 1495-1501. 10.1007/s00702-018-1904-2.
55. Forester, B.P., Berlow, Y.A., Harper, D.G., Jensen, J.E., Lange, N., Froimowitz, M.P., Ravichandran, C., Iosifescu, D.V., Lukas, S.E., Renshaw, P.F., and Cohen, B.M. (2010). Age-related changes in brain energetics and phospholipid metabolism. NMR Biomed *23*, 242-250. 10.1002/nbm.1444.
56. Anand, A., Mazur, A.C., Rosell-Arevalo, P., Franzkoch, R., Breitsprecher, L., Listian, S.A., Huttel, S.V., Muller, D., Schafer, D.G., Vormittag, S., et al. (2023). ER-dependent membrane repair of mycobacteria-induced vacuole damage. mBio *14*, e0094323. 10.1128/mbio.00943-23.
57. Mittal, E., Skowyra, M.L., Uwase, G., Tinaztepe, E., Mehra, A., Koster, S., Hanson, P.I., and Philips, J.A. (2018). Mycobacterium tuberculosis Type VII Secretion System Effectors Differentially Impact the ESCRT Endomembrane Damage Response. mBio *9*. 10.1128/mBio.01765-18.
58. Bussi, C., Heunis, T., Pellegrino, E., Bernard, E.M., Bah, N., Dos Santos, M.S., Santucci, P., Aylan, B., Rodgers, A., Fearns, A., et al. (2022). Lysosomal damage drives mitochondrial proteome remodelling and reprograms macrophage immunometabolism. Nat Commun *13*, 7338. 10.1038/s41467-022-34632-8.
59. Molliex, A., Temirov, J., Lee, J., Coughlin, M., Kanagaraj, A.P., Kim, H.J., Mittag, T., and Taylor, J.P. (2015). Phase separation by low complexity domains promotes stress granule assembly and drives pathological fibrillization. Cell *163*, 123-133. 10.1016/j.cell.2015.09.015.
60. Reineke, L.C., and Neilson, J.R. (2019). Differences between acute and chronic stress granules, and how these differences may impact function in human disease. Biochem Pharmacol *162*, 123-131. 10.1016/j.bcp.2018.10.009.

61. Anderson, P., Kedersha, N., and Ivanov, P. (2015). Stress granules, P-bodies and cancer. Biochim Biophys Acta *1849*, 861-870. 10.1016/j.bbagrm.2014.11.009.
62. Ash, P.E., Vanderweyde, T.E., Youmans, K.L., Apicco, D.J., and Wolozin, B. (2014). Pathological stress granules in Alzheimer's disease. Brain Res *1584*, 52-58. 10.1016/j.brainres.2014.05.052.
63. Piper, P.W. (1993). Molecular events associated with acquisition of heat tolerance by the yeast Saccharomyces cerevisiae. FEMS Microbiol Rev *11*, 339-355. 10.1111/j.1574-6976.1993.tb00005.x.
64. Felle, H.H. (2001). pH: Signal and messenger in plant cells. Plant Biology *3*, 577-591. DOI 10.1055/s-2001-19372.
65. Hamakawa, H., Murashita, J., Yamada, N., Inubushi, T., Kato, N., and Kato, T. (2004). Reduced intracellular pH in the basal ganglia and whole brain measured by 31P-MRS in bipolar disorder. Psychiatry Clin Neurosci *58*, 82-88. 10.1111/j.1440-1819.2004.01197.x.
66. Mandal, P.K., Akolkar, H., and Tripathi, M. (2012). Mapping of hippocampal pH and neurochemicals from in vivo multi-voxel 31P study in healthy normal young male/female, mild cognitive impairment, and Alzheimer's disease. J Alzheimers Dis *31 Suppl 3*, S75-86. 10.3233/JAD-2012-120166.
67. Kroschwald, S., Munder, M.C., Maharana, S., Franzmann, T.M., Richter, D., Ruer, M., Hyman, A.A., and Alberti, S. (2018). Different Material States of Pub1 Condensates Define Distinct Modes of Stress Adaptation and Recovery. Cell Reports *23*, 3327-3339. 10.1016/j.celrep.2018.05.041.
68. Iserman, C., Altamirano, C.D., Jegers, C., Friedrich, U., Zarin, T., Fritsch, A.W., Mittasch, M., Domingues, A., Hersemann, L., Jahnel, M., et al. (2020). Condensation of Ded1p Promotes a Translational Switch from Housekeeping to Stress Protein Production. Cell *181*, 818-+. 10.1016/j.cell.2020.04.009.
69. Franzmann, T.M., Jahnel, M., Pozniakovsky, A., Mahamid, J., Holehouse, A.S., Nuske, E., Richter, D., Baumeister, W., Grill, S.W., Pappu, R.V., et al. (2018). Phase separation of a yeast prion protein promotes cellular fitness. Science *359*. 10.1126/science.aao5654.
70. Tesei, G., Schulze, T.K., Crehuet, R., and Lindorff-Larsen, K. (2021). Accurate model of liquid-liquid phase behavior of intrinsically disordered proteins from optimization of single-chain properties. Proc Natl Acad Sci U S A *118*. 10.1073/pnas.2111696118.
71. Schuster, B.S., Dignon, G.L., Tang, W.S., Kelley, F.M., Ranganath, A.K., Jahnke, C.N., Simpkins, A.G., Regy, R.M., Hammer, D.A., Good, M.C., and Mittal, J. (2020). Identifying sequence perturbations to an intrinsically disordered protein that determine its phase-separation behavior. Proc Natl Acad Sci U S A *117*, 11421-11431. 10.1073/pnas.2000223117.
72. Pak, C.W., Kosno, M., Holehouse, A.S., Padrick, S.B., Mittal, A., Ali, R., Yunus, A.A., Liu, D.R., Pappu, R.V., and Rosen, M.K. (2016). Sequence Determinants of Intracellular Phase Separation by Complex Coacervation of a Disordered Protein. Mol Cell *63*, 72-85. 10.1016/j.molcel.2016.05.042.
73. Das, R.K., and Pappu, R.V. (2013). Conformations of intrinsically disordered proteins are influenced by linear sequence distributions of oppositely charged residues. Proc Natl Acad Sci U S A *110*, 13392-13397. 10.1073/pnas.1304749110.
74. Anderson, P., and Kedersha, N. (2008). Stress granules: the Tao of RNA triage. Trends Biochem Sci *33*, 141-150. 10.1016/j.tibs.2007.12.003.
75. Youn, J.Y., Dunham, W.H., Hong, S.J., Knight, J.D.R., Bashkurov, M., Chen, G.I., Bagci, H., Rathod, B., MacLeod, G., Eng, S.W.M., et al. (2018). High-Density

Proximity Mapping Reveals the Subcellular Organization of mRNA-Associated Granules and Bodies. Mol Cell *69*, 517-532 e511. 10.1016/j.molcel.2017.12.020.
76. Tauber, D., Tauber, G., and Parker, R. (2020). Mechanisms and Regulation of RNA Condensation in RNP Granule Formation. Trends Biochem Sci *45*, 764-778. 10.1016/j.tibs.2020.05.002.
77. Van Treeck, B., and Parker, R. (2018). Emerging Roles for Intermolecular RNA-RNA Interactions in RNP Assemblies. Cell *174*, 791-802. 10.1016/j.cell.2018.07.023.
78. Parker, D.M., Tauber, D., and Parker, R. (2025). G3BP1 promotes intermolecular RNA-RNA interactions during RNA condensation. Mol Cell *85*, 571-584 e577. 10.1016/j.molcel.2024.11.012.
79. Trussina, I., Hartmann, A., Desroches Altamirano, C., Natarajan, J., Fischer, C.M., Aleksejczuk, M., Ausserwoger, H., Knowles, T.P.J., Schlierf, M., Franzmann, T.M., and Alberti, S. (2025). G3BP-driven RNP granules promote inhibitory RNA-RNA interactions resolved by DDX3X to regulate mRNA translatability. Mol Cell *85*, 585-601 e511. 10.1016/j.molcel.2024.11.039.
80. Lyke, D.R., Dorweiler, J.E., and Manogaran, A.L. (2019). The three faces of Sup35. Yeast *36*, 465-472. 10.1002/yea.3392.
81. Li, M.Z., and Elledge, S.J. (2012). SLIC: a method for sequence- and ligation-independent cloning. Methods Mol Biol *852*, 51-59. 10.1007/978-1-61779-564-0_5.
82. Cowieson, N.P., Edwards-Gayle, C.J.C., Inoue, K., Khunti, N.S., Doutch, J., Williams, E., Daniels, S., Preece, G., Krumpa, N.A., Sutter, J.P., et al. (2020). Beamline B21: high-throughput small-angle X-ray scattering at Diamond Light Source. J Synchrotron Radiat *27*, 1438-1446. 10.1107/S1600577520009960.
83. Panjkovich, A., and Svergun, D.I. (2018). CHROMIXS: automatic and interactive analysis of chromatography-coupled small-angle X-ray scattering data. Bioinformatics *34*, 1944-1946. 10.1093/bioinformatics/btx846.
84. Manalastas-Cantos, K., Konarev, P.V., Hajizadeh, N.R., Kikhney, A.G., Petoukhov, M.V., Molodenskiy, D.S., Panjkovich, A., Mertens, H.D.T., Gruzinov, A., Borges, C., et al. (2021). ATSAS 3.0: expanded functionality and new tools for small-angle scattering data analysis. J Appl Crystallogr *54*, 343-355. 10.1107/S1600576720013412.
85. Konarev, P.V., Volkov, V.V., Sokolova, A.V., Koch, M.H.J., and Svergun, D.I. (2003). :: a Windows PC-based system for small-angle scattering data analysis. Journal of Applied Crystallography *36*, 1277-1282. 10.1107/S0021889803012779.
86. Svergun, D.I. (1992). Determination of the Regularization Parameter in Indirect-Transform Methods Using Perceptual Criteria. Journal of Applied Crystallography *25*, 495-503. Doi 10.1107/S0021889892001663.
87. Volkov, V.V., and Svergun, D.I. (2003). Uniqueness of shape determination in small-angle scattering. Journal of Applied Crystallography *36*, 860-864. 10.1107/S0021889803000268.
88. Panjkovich, A., and Svergun, D.I. (2016). SASpy: a PyMOL plugin for manipulation and refinement of hybrid models against small angle X-ray scattering data. Bioinformatics *32*, 2062-2064. 10.1093/bioinformatics/btw071.
89. Schindelin, J., Arganda-Carreras, I., Frise, E., Kaynig, V., Longair, M., Pietzsch, T., Preibisch, S., Rueden, C., Saalfeld, S., Schmid, B., et al. (2012). Fiji: an open-source platform for biological-image analysis. Nat Methods *9*, 676-682. 10.1038/Nmeth.2019.

STAR Methods

Experimental model and study participant details

Escherichia coli strains

Recombinant proteins were expressed in *Escherichia coli* BL21(T7 Express lysY/Iq) host cells, grown in terrific broth (TB) medium at 25°C, 220 rpm.

Method details

Cloning, protein expression and purification

The DNA fragment encoding full-length human G3BP1 was PCR-amplified from a U2OS cDNA library and subsequently subcloned into the pET30 vector using ligation-independent cloning.[81] To facilitate purification, a TEV cleavage site was introduced between the N-terminal poly-His6 tag and G3BP1. The final construct, termed his6-TEV-G3BP1, was validated by DNA sequencing (Eurofins Genomics) and served as the template for constructing the G3BP1 deletion mutants used in this study. The expression constructs of his6-TEV-NTF2L (residues 1-139), his6-TEV-NTF2LA (residues 1-232), his6-TEV-G3BP1ΔRGG (residues 1-413) and his6-EGFP-TEV-G3BP1 were created using the same cloning method and verified by DNA sequencing.

Full-length recombinant G3BP1 was expressed in T7 Express lysY/Iq competent *E. coli* cells at 25°C overnight in terrific broth (TB) and purified under native conditions. Bacteria cells were grown to an OD of approximately 0.7 in TB medium and induced with 0.5 mM IPTG at 25 °C overnight, then pelleted and re-suspended in lysis buffer containing 50 mM HEPES (pH 7.5), 300 mM NaCl, 1 mM DTT, complete protease inhibitor cocktail tablet (Roche), and benzonase (Millipore). Cells were lysed by sonication (10 minutes, 40% amplitude, 5 seconds on, 5 seconds off). Following centrifugation to remove cell debris, the clarified supernatant was applied to Ni-NTA agarose resin (QIAGEN). The eluent was collected, and the poly-His tag was removed by TEV protease (PSF, KI, Stockholm) in HEPES buffer containing 0.5 mM EDTA and 1 mM DTT. The cleaved protein was passed through the Ni-NTA column as flow-through. Subsequently, G3BP1 was loaded onto a HiTrap Heparin HP affinity column (Cytiva) to eliminate non-specific RNA binding. The fractions were analyzed by SDS-PAGE, and the corresponding tubes containing G3BP1 were pooled and concentrated. Full-length G3BP1 was purified using a Superdex 200 increase10/300 GL column (Cytiva) in the desired buffers for SAXS studies. The monodisperse G3BP1 fractions were concentrated, filtered, flash frozen in liquid nitrogen, and stored at −80°C. His6-TEV-G3BP1(ΔRGG) (residues 1-413) and his6-EGFP-TEV-G3BP1 were purified using similar protocols. To assess the degree of polydispersity of the freshly purified proteins, DLS was performed and the hydrodynamic diameter of the proteins was determined (**Figures S1C, S3C and S5B**).

Deletion constructs NTF2L and NTF2LA were purified as previously described.[36] Briefly, the NTF2L dimer was affinity-purified using Ni-NTA agarose resin and isolated via Superdex 75 10/300 GL size exclusion chromatography (GE Healthcare). Following TEV cleavage, NTF2L was collected as the Ni-NTA flow-through. Both NTF2L and NTF2LA were further purified using a Superdex 75 10/300 GL column after tag removal to enhance purity. Protein-containing fractions were pooled and concentrated using 10 kDa MWCO Amicon ultra centrifugal filters (Millipore).

Small Angle X-ray Scattering (SAXS)

SAXS data were recorded at the B21 beamline of the Diamond Light Source (Didcot, United Kingdom)[82]. Data collection occurred at 3-second intervals using an EigerX 4M detector (Dectris, Switzerland) at a sample detector distance of 3.7 m and at a wavelength of λ = 0.09464 nm (I(s) vs s, where $s = 4\pi^{*}\sin\theta/\lambda$, and 2θ is the scattering angle), with fixed energy at 13.1 keV, covering the scattering vector range from 0.045 to 3.4 nm^{-1}.

For the SEC-SAXS runs of G3BP1, an Agilent 1200 HPLC system equipped with a Superdex 200 increase 3.2/300 column (Cytiva) was used. 60 µL of the samples was injected and run at flow rate of 0.075 ml/min in indicated buffer. The SEC-separated sample was then exposed to X-rays in a 1.5-mm diameter, 10-µm-thick quartz capillary flow cell. The running buffer was supplemented with 1 % glycerol to mitigate radiation damage, samples and the corresponding matched solvent blank were measured.

SAXS data processing and modeling

Initial SEC-SAXS datasets were processed using Chromixs,[83] both automatically and interactively, resulting in buffer subtracted curves. Further data processing was then performed with the ATSAS 3.1 suite.[84] The radius of gyration (R_g) were obtained by fitting the linear Guinier region of the data using PRIMUS.[85] The pair distribution function, p(r), was generated with GNOM[86] and was used to determine the D_{max}. Molecular weight was estimated from Porod volume determination. *Ab initio* models of molecular envelopes were generated using DAMMIF,[48] where scattering from the calculated envelopes was fitted against the experimental curves and evaluated by the χ^2 values. The resulting twenty *ab initio* models were averaged with DAMAVER.[87] Advance hybrid modeling using available high resolution parts of the structure with addition of the missing loops/domains was conducted with CORAL.[49] A SASpy plugin in PyMOL[88] was employed to overlay the dimeric NTF2L X-ray structure with the corresponding *ab initio* models.

The SAXS data are summarized in Table 1 and the respective curves and models have been deposited into SASBDB[50].

In vitro liquid–liquid phase separation (LLPS) assays

For G3BP1-RNA condensate formation, 5 µM of EGFP-G3BP1 or 25 µM of untagged protein sample were incubated with or without purified total RNA at varied buffer conditions. Total RNA was isolated from U2OS cells by TRIzol® reagent (Invitrogen, USA) and quantified with a Thermo Scientific NanoDrop 2000 spectrophotometer. Typically, 50 ng/µL total RNA was added to induce LLPS of G3BP1. The samples were mixed in low binding tubes (COSTAR 3206) and transferred to a 384-well ultra-low attachment microplate (Greiner Bio-one, Germany) at room temperature. Phase separation was visualized using a Nikon CrEST X-Light V3 Confocal Microscope equipped with a 20× air objective, controlled by NIS-Elements software. For EGFP-G3BP1 condensates, the spinning disk configuration with 488 nm excitation was employed, with an ROI of 1024 x 1024 pixels to facilitate

rapid imaging and minimize photobleaching. Imaging of untagged G3BP1 condensates was conducted using a camera-TL for high resolution, focusing on a region of interest (ROI) measuring 610 x 640 pixels. Condensates were imaged with identical settings between replicates to allow for comparison of granule intensities. Images were captured within 10 minutes after mixing the protein, RNA and the indicated buffer, acquired as Z-stacks with a step size of 6–8 μm over a total depth of 200 μm (25–30 Z-planes per stack). Maximum intensity projections of the Z-stack images and subsequent quantitative analyses were performed using semi-automated workflows Fiji.[89] Scale bars were added through Analyze → Tools → Scale Bar function of Fiji. Three independent LLPS assays are performed.

Dynamic light scattering (DLS)

Dynamic light scattering of protein samples was performed at 25°C with a Zetasizer Ultra instrument (Malvern Panalytical) using side scattering. Protein samples were mounted using 1.0 × 1.0 mm disposable cuvette capillaries (Malvern Panalytical) and placed within a low-volume disposable sizing cell kit holder (Malvern Panalytical). Typically, 5 μL of a 5 μM protein sample were tested under the indicated pH and salt buffer conditions. Each experiment was repeated at least three times. Monodispersity and statistical size distribution were analyzed using the manufacturer supplied ZS Xplorer software.

Quantification and statistical analysis

Statistical analyses of in vitro LLPS were performed using semi-automated workflows in Fiji. Particle size distribution analyses were performed using a Zetasizer Ultra and data were analyzed directly in the accompanying ZS Xplorer software. All statistical details, including experiments tested, n values and error measures, are provided in the figure legends and method details.

Supplemental information

Document S1. Figures S1-S6.

Figure titles and legends

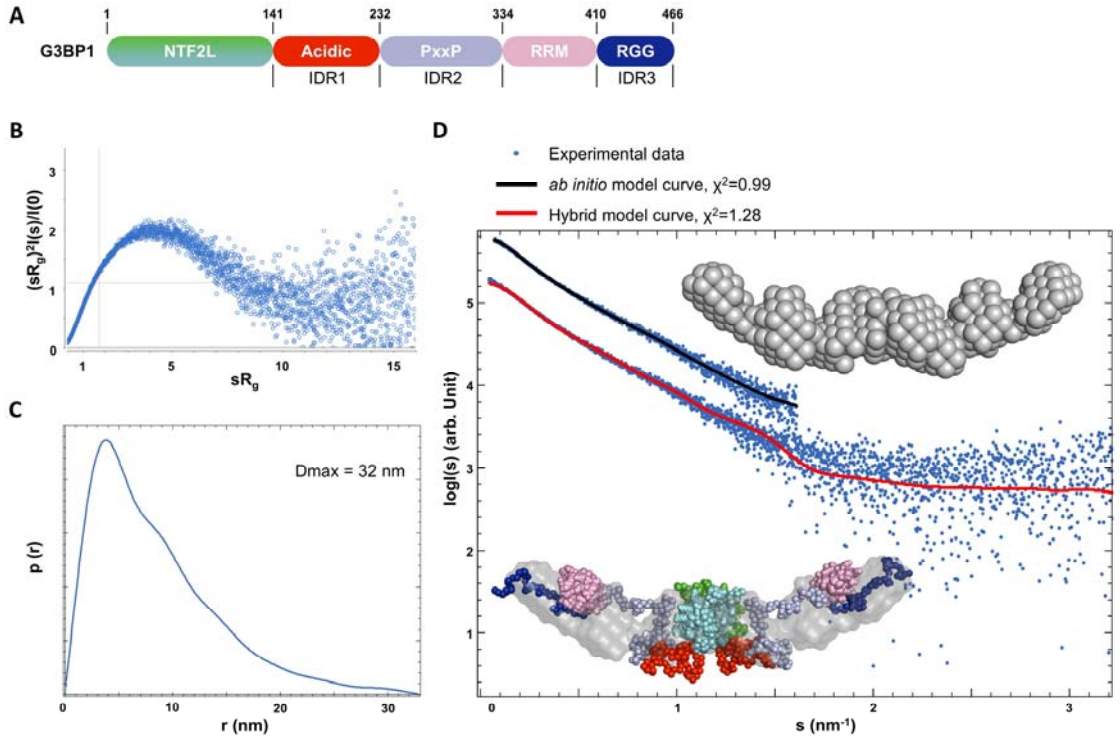

Figure 1. Full-length G3BP1 exhibits an elongated shape with a clearly defined domain architecture

A. Schematic diagram illustrating the domain organization of G3BP1, highlighting the locations of the five main domains, including the three large intrinsically disordered regions (IDRs). **B.** Scattering curve of full-length G3BP1 shown in normalized Kratky plot. **C.** Pair distance distribution functions, p(r), for full-length G3BP1 at pH 7.5. **D.** The *ab initio* model of full-length G3BP1 (generated with DAMMIF) is presented in the upper inset as grey spheres. The black line describes the fit of the *ab initio* model with restricted angular range of the SAXS data. The SAXS-based hybrid model of full-length G3BP1 is presented in the lower inset, with the domains colored as indicated in Fig. 1A. The fit shown by the red curve shows good agreement with the experimental data. Overlay of the hybrid model of G3BP1 and the *ab initio* model (50% transparency) is presented in the lower inset. Curves have been shifted along the y-axis for better visibility. The buffer conditions for these analyses were 20 mM Tris, pH 7.5, and 150 mM NaCl. The scattering data is displayed as a function of the momentum transfer $s = 4\pi^{*}\sin\theta/\lambda$, where $\lambda = 0.09464$ nm is the wavelength and 2θ is the scattering angle.

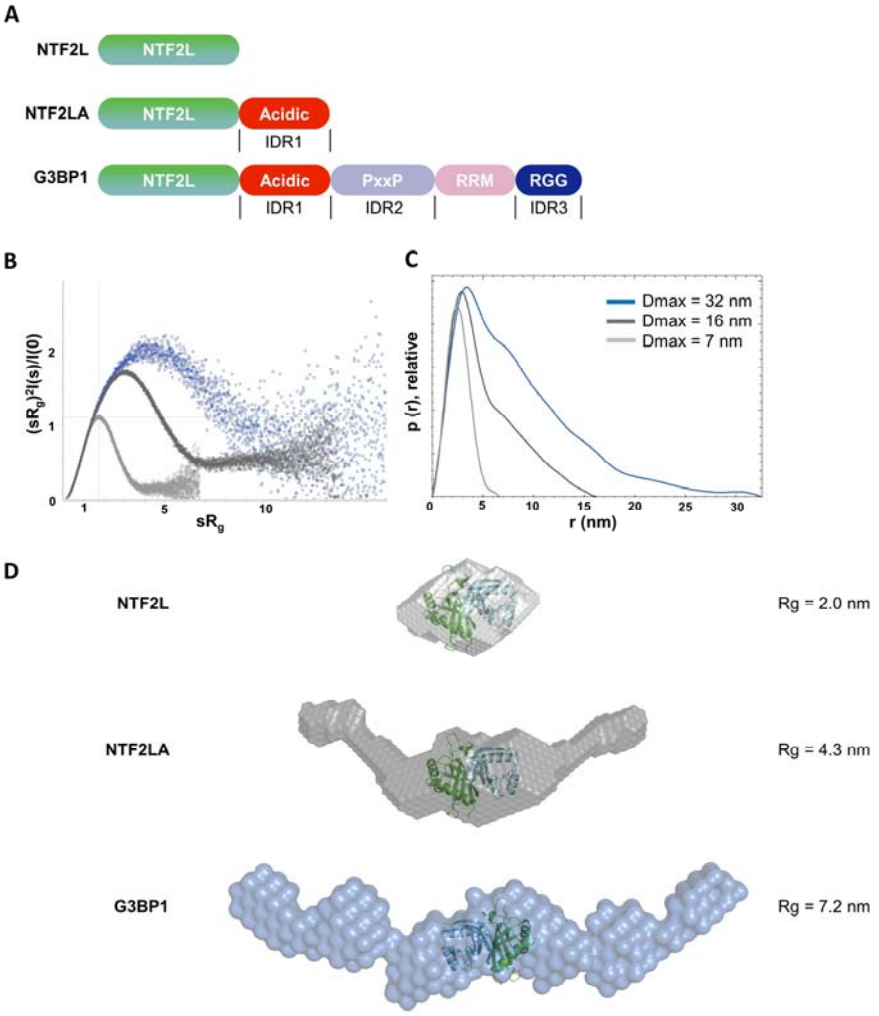

Figure 2. Comparative SEC-SAXS analyses of full-length and truncated G3BP1 variants confirm that G3BP1 forms a head-to-head antiparallel dimer

A. Schematic diagrams illustrating the domain organizations of NTF2L, NTF2LA and full-length G3BP1. **B.** Scattering curves of three samples shown in normalized Kratky plots. **C.** Distance probability functions, p(r) of the three samples, reveal distinct shapes and sizes for each construct. NTF2L is shown in light gray, NTF2LA in dark gray and full-length G3BP1 in blue. **D.** Overlay of the NTF2L dimeric crystal structure (PDB code 6TA7) onto the *ab initio* reconstructions. *Ab initio* models are presented as spheres highlighting the structural similarities between NTF2LA and the central region of full-length G3BP1. SAXS data collected in buffer 20 mM Tris and 150 mM NaCl, pH 7.5.

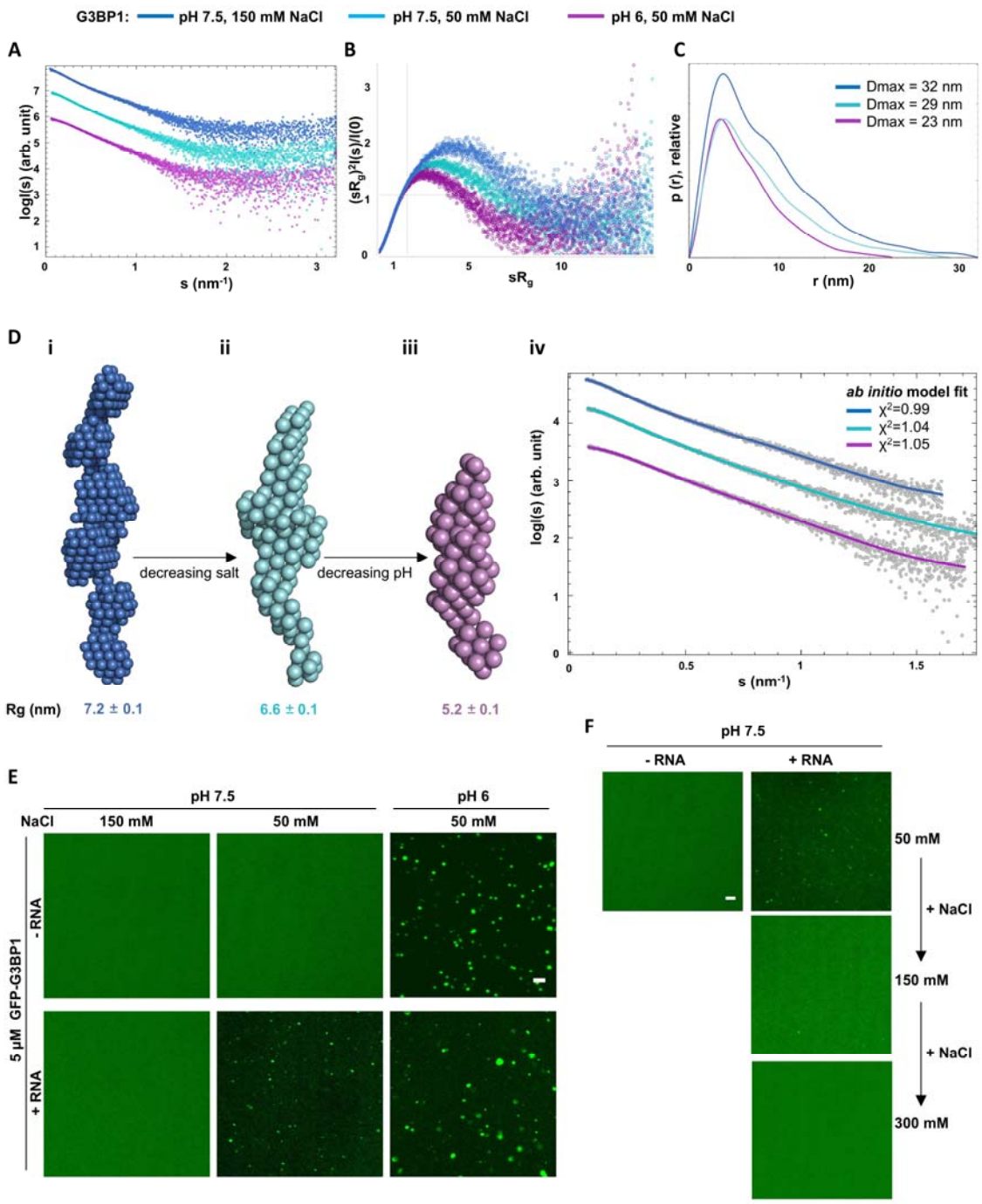

Figure 3. Full-length G3BP1 undergoes substantial conformational shifts in response to changes in pH and salt concentration

A. Final scattering profiles of full-length G3BP1 under three buffer conditions. Curves have been shifted along the intensity axis for better visibility. **B.** Normalized Kratky plots representation of G3BP1 at three different buffer conditions. **C.** p(r) function of the three full-length G3BP1 samples. **D.** *Ab initio* models (generated with DAMMIF) are presented as beads (i, ii and iii). (iv) The fits of scattering curves with respective *ab initio* models. **E.** *In vitro* LLPS assays were performed and fluorescence images

of G3BP1 (5 μM) with or without total RNA (50 ng/μL) under varied buffer conditions are presented. **F.** Fluorescence images of G3BP1-RNA condensates were captured while gradually increasing the NaCl concentration from 50 mM to 300 mM. Scale bar represents 10 μm.

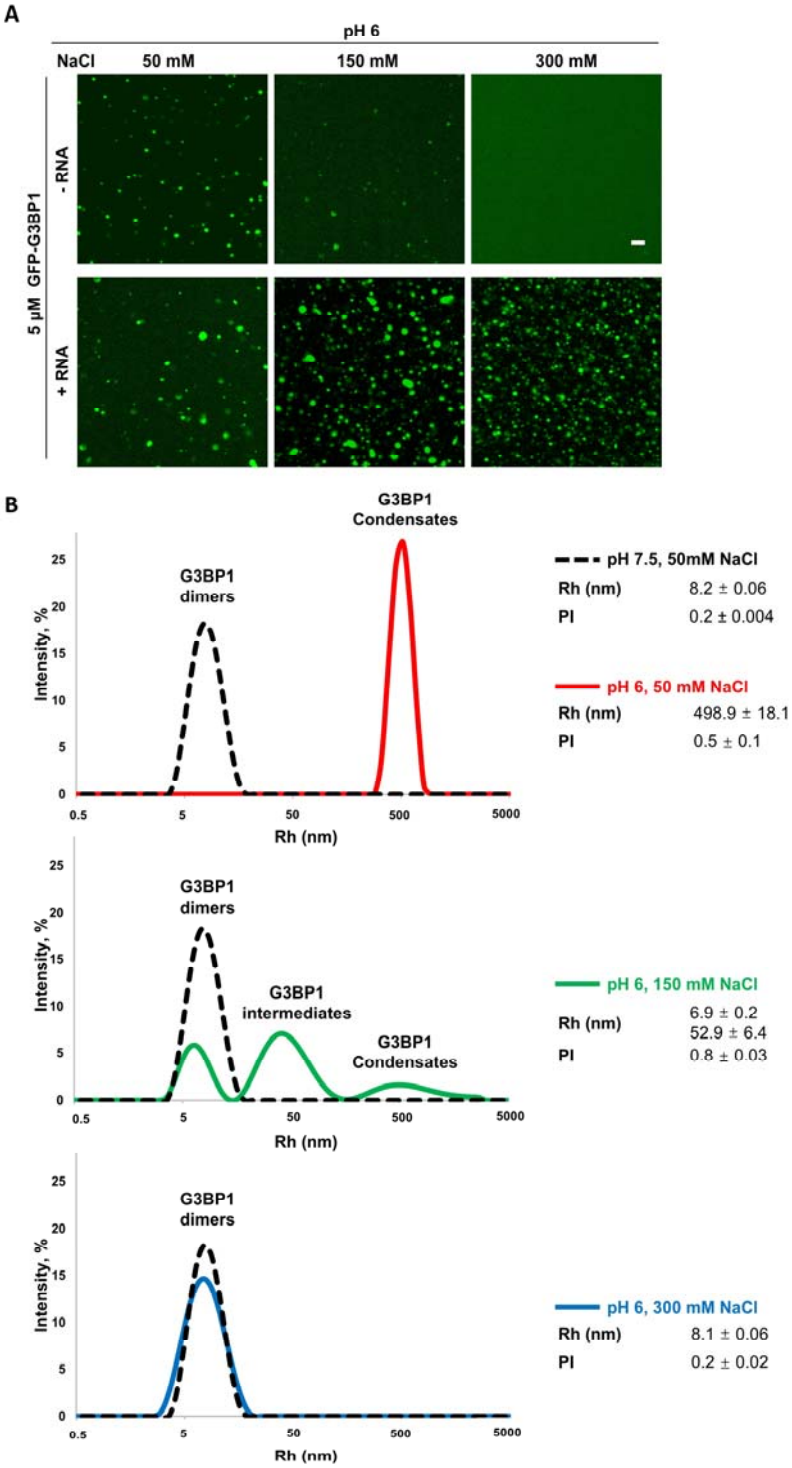

Figure 4. RNA-independent G3BP1 phase separation is observed at pH 6.0

A. *In vitro* LLPS assay: fluorescence images of G3BP1 (5 µM) with or without total RNA (50 ng/µL) at pH 6.0, under various salt conditions. Scale bar represents 10 µm. **B.** DLS measurements of the oligomeric species of G3BP1 at pH 6.0 across different salt concentrations, illustrating particle size distribution (mean by intensity) profiles. DLS data of G3BP1 collected at pH 7.5, 50 mM NaCl (black dashed lines) are included as control.

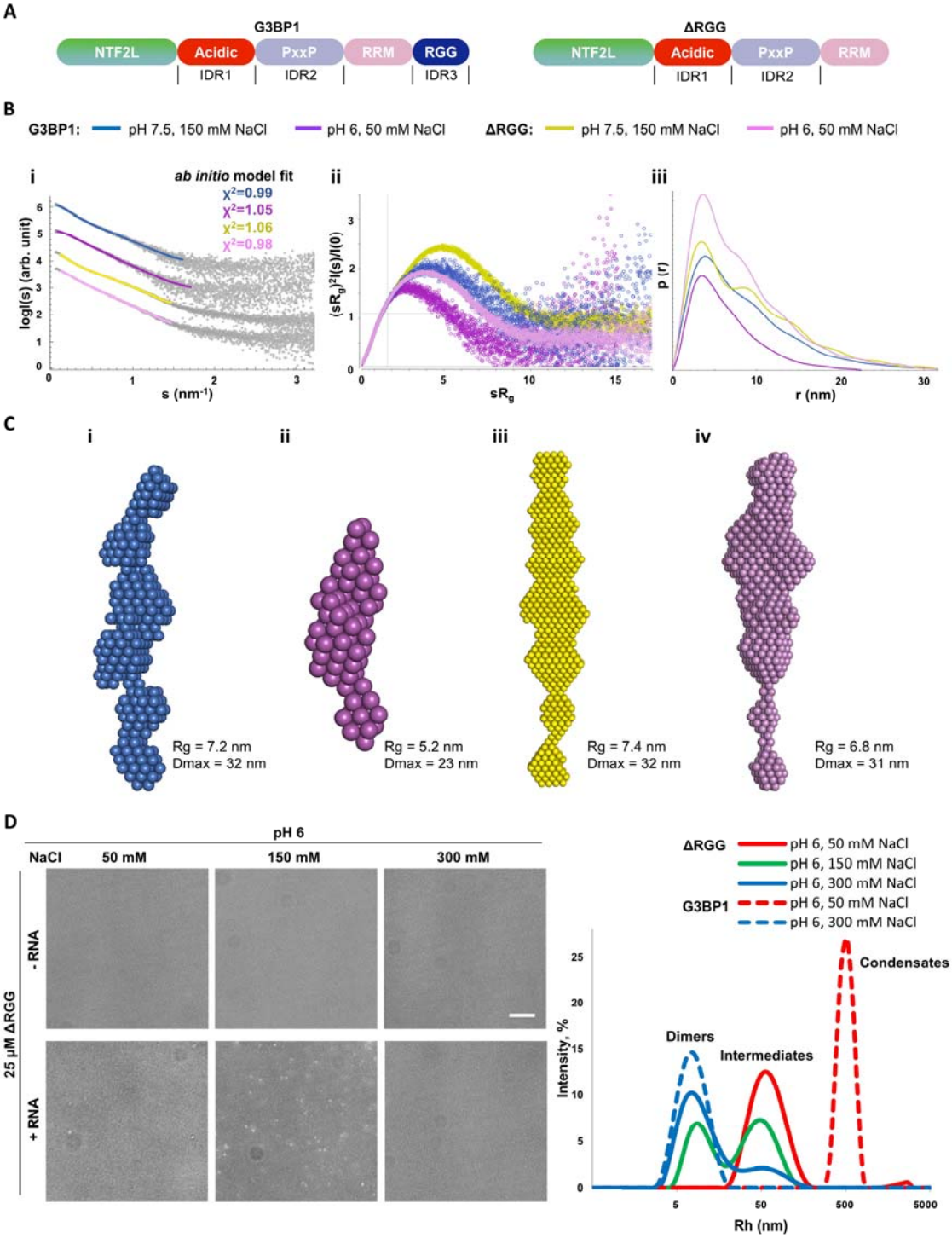

Figure 5. Elimination of the RGG domain mitigates the influence of salt and pH modifications on the compactness of G3BP1

SEC-SAXS and *in vitro* LLPS analyses of full-length G3BP1 and G3BP1-ΔRGG. **A.** Schematic diagrams illustrating the domain organizations of G3BP1 and G3BP1-ΔRGG. **B.** SEC-SAXS analyses are presented in (i) scattering profiles and fits, curves have been shifted along the y-axis for better visibility, (ii) normalized Kratky

plots and (iii) distance probability functions, p(r). **C.** *Ab initio* models (generated with DAMMIF) are presented as spheres, indicating significant changes in shape and size for full-length G3BP1 under reduced pH and salt concentrations (i and ii), in contrast to G3BP1-ΔRGG (iii and iv). **D.** *In vitro* LLPS assays showing the capacity of purified recombinant G3BP1-ΔRGG (25 μM) to form droplets/condensates with or without 50 ng/μL total RNA at pH 6.0, and varying NaCl concentrations. Scale bar represents 10 μm. **E.** Aligned DLS measurements of the oligomeric species of G3BP1 (solid lines) and G3BP1-ΔRGG (dashed lines) at pH 6.0, across varied salt concentrations, reveal that removal of the RGG domain disallows the formation of larger condensates.

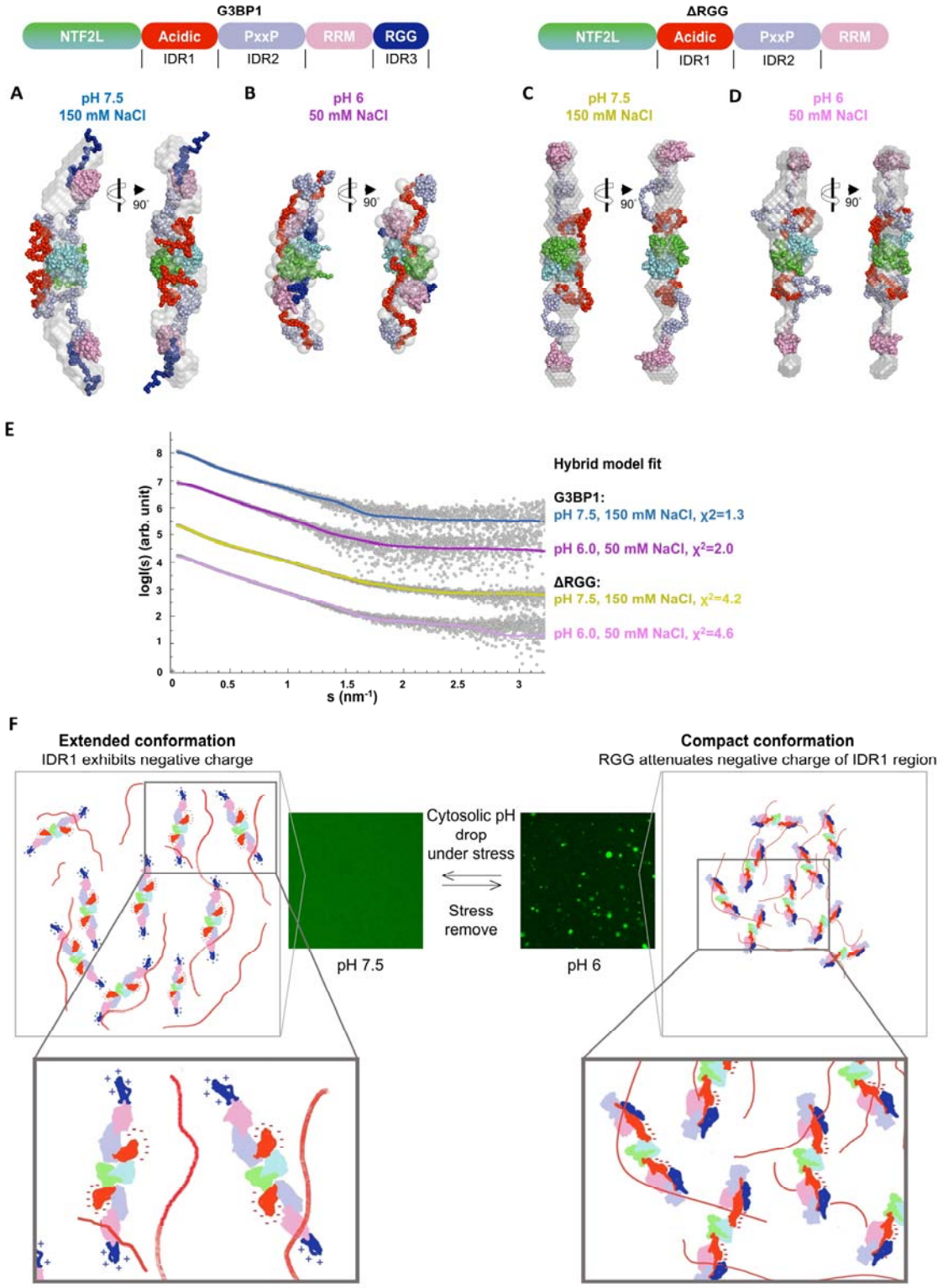

Figure 6. Hybrid models of G3BP1 and G3BP1(ΔRGG) indicate domain re-arrangement induced by environmental conditions

Overlay of each hybrid model (represented as beads) on the corresponding *ab initio* model (transparent surface). At each indicated buffer condition, a representative

hybrid model of G3BP1 (**A, B**) and G3BP1(ΔRGG) (**C, D**) is presented, with the domains colored as in the schematic diagrams. **E.** SEC-SAXS profiles and respective hybrid body model fits. **F.** A scheme of conformational rearrangements in G3BP1 regulating SG nucleation in response to microenvironment changes. Full-length G3BP1 adopts an expanded conformation (left panel) in the resting state, with the RRM and RGG domains stretching away from the centrally localized NTFL2 dimer. The highly negatively charged IDR1 inhibits G3BP1 phase separation by repelling neighboring G3BP1-RNA molecules, disallowing SG network formation. Upon stress, untranslated mRNAs are released and accumulated, potentially reducing the local cytoplasmic pH and provoking domain rearrangements in G3BP1 leading to a compact conformation (right panel). The RGG region effectively neutralizes the inhibitory role of IDR1, facilitating the nucleation process, and thereafter the formation of SGs.